Decomposition of atmospheric aerosol phase function by particle size and asphericity from measurements of single particle optical scattering patterns

Kevin B. Aptowicz [a],[*], Yong-Le Pan [b], Sean D. Martin [a], Elena Fernandez [c], Richard K. Chang [d], Ronald G. Pinnick [b],[c]

[a] Department of Physics, West Chester University, West Chester, PA 19383, USA
[b] US Army Research Laboratory, 2800 Powder Mill Road, Adelphi, MD 20783, USA
[c] Department of Physics, New Mexico State University, Las Cruces, NM 88003, USA
[d] Department of Applied Physics, Yale University, New Haven, CT 06511, USA

A R T I C L E   I N F O

A B S T R A C T

We demonstrate an experimental approach that provides insight into how particle size and shape affect the scattering phase function of atmospheric aerosol particles. Central to our approach is the design of an apparatus that measures the forward and backward scattering hemispheres (scattering patterns) of individual atmospheric aerosol particles in the coarse mode range. We captured over 30 000 scattering patterns during winter (January 2007) at an urban site in Las Cruces, NM. The size and shape of each particle is discerned from the corresponding scattering pattern. In particular, autocorrelation analysis is used to differentiate between spherical and non-spherical particles, the calculated asphericity factor is used to characterize the morphology of non-spherical particles, and the integrated irradiance is used for particle sizing. We found that the fraction of spherical particles decays exponentially with particle size, decreasing from 11% for particles on the order of 1 μm to less than 1% for particles over 5 μm. The average phase functions of subpopulations of particles, grouped by size and morphology, are determined by averaging their corresponding scattering patterns. The phase functions of spherical and non-spherical atmospheric particles are shown to diverge with increasing size. In addition, the phase function of non-spherical particles is found to vary little as a function of the asphericity factor. Our results support the current remote sensing practice of characterizing atmospheric aerosol particles as a composition of spherical and non-spherical particles with less concern about the diversity of morphology within non-spherical particles. In addition, our results suggest that assuming a constant spherical fraction independent of particle size may not accurately reflect the real morphological distribution of atmospheric aerosol particles.

1. Introduction

Atmospheric aerosol particles impact our Earth's climate by scattering and absorbing radiation as well as by modifying the radiative properties of clouds [1]. Modeling and quantifying this contribution to the Earth's energy balance are needed for climate research. However, the specific contribution of atmospheric aerosols to the Earth's climate is largely unknown and represents a major source of uncertainty in climate models [2]. This uncertainty is driven in part by a lack of knowledge of the global spatio-temporal distribution of atmospheric particles and in part by inadequate modeling of the optical properties (i.e. scattering and absorption) of atmospheric aerosol

* Corresponding author. Tel.: +1 1 610 436 3010.
  E-mail address: kaptowicz@wcupa.edu (K.B. Aptowicz).

particles [3]. These two sources of uncertainty are connected since remote sensing data collected to determine spatio-temporal distribution of atmospheric particles is inverted using assumed optical properties of atmospheric aerosol particles [4]. Therefore, an accurate description of the optical properties of atmospheric aerosol particles is critical to reducing uncertainties in climate research.

The diverse range of particle morphologies makes characterization of the optical properties of atmospheric aerosol particles a challenging endeavor. A common approach is to model aerosol particles using simple shapes in which the optical properties can be calculated; a distribution of these shapes is then used to model an ensemble of atmospheric particles. Because of simplicity and computational efficiency, homogeneous spheres are often used as model particles [5,6]. However, homogeneous spheres inadequately reproduce the optical properties of atmospheric aerosol particles, particularly large irregular particles like mineral dust [7–12]. A mixture of homogeneous spheroids and spheres has gained substantial traction as a model for aerosol particles ensembles and is currently being used in the inversion of AERONET (AErosol RObotic NETwork) retrievals [13]. This model works surprisingly better than other proposed shapes such as prisms [14], but more validation studies are needed. For example, it is unclear if the spheroidal model is applicable to size distributions with effect radii larger than 1 μm [4]. Furthermore, the fraction of spherical particles is often assumed to be constant for all sizes, which might not be representative of real atmospheric aerosol distributions [15]. Finally, the distribution of aspect ratios of the particles used in the spheroid model is fixed and based on a fairly small selection of measurements, and therefore may not be representative of a wider range of aerosol particles [16,17].

Atmospheric aerosol measurements can play a critical role in answering these and other key questions regarding the validation and improvement of contemporary particle modeling. Historically, atmospheric aerosol measurements involving multi-angle light scattering have proven particularly useful in the evolution of particle models. For example, the measurement of full Mueller matrices of dust collected from the Earth's surface was used to constrain and validate the current spheroidal model [8,13]. More recently, analysis of laboratory experiments combining multi-angle scattering, polarimetry, and IR extinction data has suggested that a single spheroidal shape distribution for all particles sizes is not representative of silicate clay aerosol [17]. Other experimental measurements have made similar contributions to the accuracy of particle modeling.

However, these measurements, while providing critical insight to the field of climate research (see Ref. [18]), have certain limitations since they are performed on particle ensembles; optical properties specific to single particles or even particle subpopulations are partly lost in these ensemble measurements. Recently, scattering measurements of individual atmospheric particles have emerged [19–21,15]. However, these studies focus on measuring particle morphology, specifically particle shape, without measuring optical properties, such as the scattering phase function. Thus in the field of climate research, there appear to be two disparate multi-angle light-scattering techniques, ensemble measurements that explore key optical properties for climate research and single-particle measurements that explore particle morphology needed for aerosol modeling. Neither techniques are currently capable of measuring both optical properties relevant to climate research and morphology information at the single particle level. A technique that did achieve this could decompose the optical properties of atmospheric aerosol by particle subpopulations (e.g. how the scattering phase function varies as a function of particle size and shape), which would greatly aid the validation and evolution of particle modeling thereby facilitating advances in aerosol characterization and climate modeling.

Here, we devise a powerful experimental technique that can obtain the scattering phase function of individual aerosol particles as well as capture optical information related to particle size and morphology. Essential to our approach is the measurement of two-dimensional angular optical scattering (TAOS) patterns from single atmospheric aerosol particles in the coarse mode range [22,23,15,24]. Individually, TAOS patterns provide key information about particle morphology. For example, we demonstrate how autocorrelation analysis of these TAOS patterns can identify optically smooth spherical particles and distinguish them from other particles with overall spherical shape but having rough surface or inhomogeneous distribution of refractive index. And as a collection, TAOS patterns provide ensemble-averaged optical properties. In particular, by grouping TAOS patterns based on particle size and shape, we explore how the scattering phase function depends upon particle morphology. Analysis of over 30 000 TAOS patterns collected from atmospheric aerosol particles in Las Cruces, NM, indicates (1) a decrease in the fraction of optically smooth spherical particles with increasing scattering size, (2) a divergence of the scattering phase function between spherical and non-spherical particles as particle size increases, and (3) little variation in the scattering phase function for non-spherical particles that are further classified using the asphericity factor.

2. Experiment design

The apparatus to capture two-dimensional angular optical scattering (TAOS) patterns is slightly modified from a previous design [15]. The path of the incident laser beam relative to the scattering volume is rotated by 90° so that both the forward and backward scattering hemispheres from single aerosol particles are detected [24]. Furthermore, to optimize the scattering geometry for the analysis performed in this paper, the polarization of the incident laser beam is changed from linearly polarized to circularly polarized. The remainder of the experimental geometry remains very similar to the previous design.

Briefly, aerosol was sampled through a 4-cm diameter, 3-m long, conductive hose inserted through the outside wall of a first floor laboratory (further details in Section 3). A manifold attached to this hose provided aerosol flow for two virtual impactor concentrators, one for single-particle

fluorescence spectrum measurements [25] and one for TAOS measurements. For the TAOS measurements, aerosol particles were concentrated by a concentrator (Dycor, XMX) with inlet flow of about 10 l/s and minority outlet flow of about 1 l/min. This concentrator has a size-dependent sample rate that varies from about 1 l/min for 1 μm sized particles to a maximum of approximately 100 l/min for nominal 5 μm particles, and falls off again for larger particles above 8 μm [26]. Therefore, our instrument disproportionately sampled particles around 5 μm in size as compared to those around 1 μm or 10 μm in size. The minor flow from an aerosol concentrator was drawn under slight negative pressure (∼2 mbar) into an airtight aluminum cube (18″ on each side) that houses the triggering and collection optics. A conically shaped aerodynamic sheath nozzle focused the minor flow inside the airtight box into a laminar jet around 300 μm in diameter. The aerosol nozzle tip was positioned 0.5 cm above the first focal point of the elliptical reflector. After traversing the focal point, the aerosol particles exit the airtight box through an outlet tube driven by a piston pump (KNF Neuberger, model UN05) located about 1 cm below the focal point.

To reduce errors associated with misaligned particles, only particles at or near the first focal point of the elliptical reflector are illuminated. This is achieved with a cross-beam trigger system that restricts the scattering volume to be significantly smaller than the illuminating beam [27]. In particular, two CW TEM00 diode lasers (Microlaser Systems), emitting light at 635 nm (power 25 mW) and 685 nm (40 mW), intersect at the first focal point of the elliptical reflector with beam waists of 25 μm and 13 μm respectively. This intersection defines the trigger volume and only particle traversing both these laser beams trigger the system [15]. Accounting for the aerosol concentrator and the cross-beam triggering system, the overall effective sampling rate for this TAOS system peaks at about 12 l/min for nominally 5 μ particles, decreasing to about 3 l/min for nominally 3 μ and 10 μ particles.

Fig. 1(a) depicts both the triggering optics as well as the collection optics for capturing TAOS patterns. Once a triggering event occurs, a single pulse emitted from the second harmonic output of a Nd:YAG laser (Spectra Physics, X-30, 532 nm, 30 ns pulse width) is synchronized to illuminate the detected particle at the first focal point. Light scattered from this particle reflects off the elliptical reflector, exits the airtight box through a quartz window, and is refocused to the second focal point (defined with an iris) outside the box. The prolate elliptical reflector was custom machined using single point diamond turning (10 nm resolution) to have a 4″ major diameter and 2.646″ minor diameter (Lightwave Enterprises). The light rays from the "virtual" particle located at the iris are then detected by a 1024 × 1024 ICCD detector (Andor Technology, Model ISTAR DH734-25F-03) that is also triggered by the cross-beam trigger system. The CW diode trigger beams are turned off during the intensifier "gate on" period of the ICCD (1 μs) to eliminate unwanted scattering light from the diode laser illuminations. Each pixel of the ICCD is matched with a unique scattering angle (polar scattering angle θ and azimuth scattering angle ϕ). A correction is
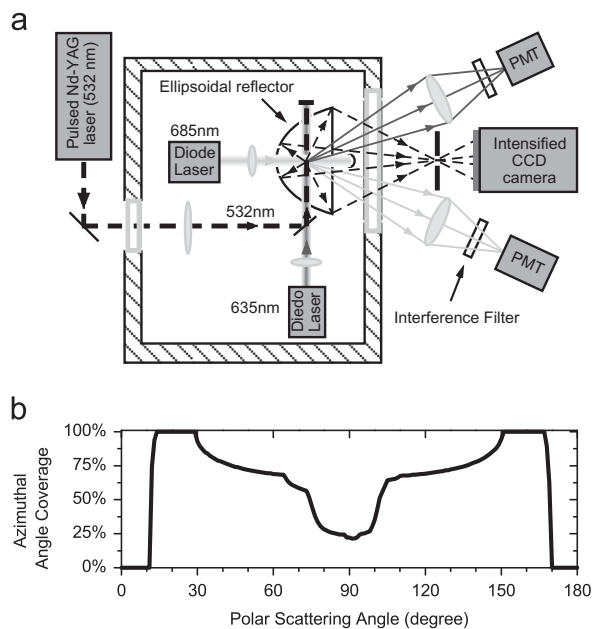

Fig. 1. (a) Schematic of TAOS instrument slightly modified from Aptowicz et al. [15] to simultaneously capture forward and backward scattering hemispheres from single aerosol particles. (b) Detected range of azimuthal angles as a function of polar scattering angle.

then applied to account for the variation in scattering solid angle spanned by each pixel. With this experimental geometry, scattered light is detected for polar scattering angle θ from 12° to 167° and azimuthal angle ϕ from 0° to 360°. However, the experimental geometry significantly reduces the azimuthal angle coverage for certain polar angles, as indicated in Fig. 1(b).

The system was tested and routinely checked with polystyrene latex (Duke Scientific) spheres. The spheres were aerosolized by a nebulizer (Royco Aerosol Generator, 256) and fed into the minor flow inlet. A TAOS pattern captured from a single sphere is projected onto spherical coordinates (θ, ϕ) and then separated into forward and backward scattering hemispheres. Fig. 2(a) shows the typical forward and backward scattering hemispheres for a 1 μm polystyrene latex sphere. For comparison, numerical simulations based on Lorenz–Mie theory are also displayed. The black regions around the outside and at the center of experimental patterns are inaccessible angles for our apparatus. The experimentally measured scattering hemispheres are in good agreement with numerical simulations. By integrating the scattering intensity over ϕ, the phase function can be calculated and compared with Mie-Theory as shown in Fig. 2(b). Fluctuations in the overall scattering intensity are evident by comparing the scattering from individual polystyrene latex spheres. This fluctuation corresponds to a variation in the intensity of the incident beam illuminating the particles from shot-to-shot. We did not correct for this variation. Both the individual and average phase functions match well with predictions based on Lorenz–Mie theory, although some smoothing is evident.
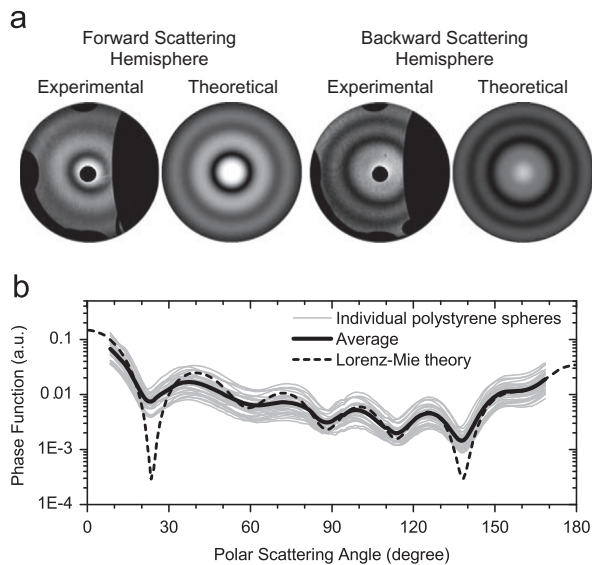
a

b

Fig. 2. (a) Forward and backward scattering hemispheres for a 1 μm polystyrene sphere from experiment and calculated from Lorenz–Mie theory. Black regions in experimental image represent inaccessible angles for our experimental geometry. (b) Phase functions obtained from 30 different polystyrene spheres (gray solid lines) compared with Lorenz–Mie theory (dashed line). Black solid line indicates the average scattering intensity for all 30 spheres.

3. Data collection

Measurements were conducted on the campus of New Mexico State University, Las Cruces, New Mexico (32.2°N latitude; elevation 1200 m) during January 2007. Las Cruces is located in the Chihuahuan Desert of the southwestern US and northern Mexico. It is a moderately populous urban area (metropolitan-area population about 200 000) with relatively low precipitation of about 25 cm per year. The metroplex of El Paso, Texas – Ciudad Juarez, Mexico is located 80 km to the south. In January, dusty conditions are generally low and the total aerosol loadings are approximately 10 μg/m³ or below with about one percent black carbon aerosol loading [28]. Aerosol was sampled about 2 m above ground level through the wall of a 3-story building on campus. A somewhat heavily traveled auto thoroughfare (i.e. University Avenue) is located 105 m north from the sample site. These measurements were carried out simultaneously with single-particle fluorescence spectrum measurements that shared the same aerosol inlet. Further details and discussion of those measurements can be found in Ref. [25].

Data collection occurred between 5 pm on January 21st, 2007, and 5 am on January 23rd, 2007, during which temperature varied from −1 °C to 8 °C and relative humidity varied from 50% to 93%. Over this period, 38 801 TAOS patterns of atmospheric aerosols were captured. Each TAOS pattern is analyzed using an image analysis routine written in Matlab (Mathworks) and kept if two criteria are met. First, the measured irradiance has to remain within the dynamic range of the ICCD. Thus large particles that saturate the ICCD are discarded from analysis. Second, the alignment of the particle within the ellipsoidal reflector is

evaluated by the spatial location of the experimental artifacts in the TAOS patterns. For perfectly aligned particles, these experimental artifacts should not vary in the TAOS patterns. TAOS patterns in which the particle is obviously misaligned are discarded. After applying these filtering criteria, 31 407 TAOS patterns of atmospheric aerosol particles are kept from the data collection.

Scanning electron microscope images of atmospheric particles collected during the data collection suggest a diverse range of particle morphology as shown in Fig. 3(a). The detected TAOS patterns were also diverse as shown in Fig. 4. The actual particle morphology of the atmospheric particles that generated these individual TAOS patterns is unknown. However, particle shape and internal structure can be postulated from the TAOS patterns. For example, with the appearance of concentric rings in both the forward and backward scattering hemispheres, Fig. 4(a) is most likely a homogeneous sphere. In contrast, the broken ring structure in the backward scattering
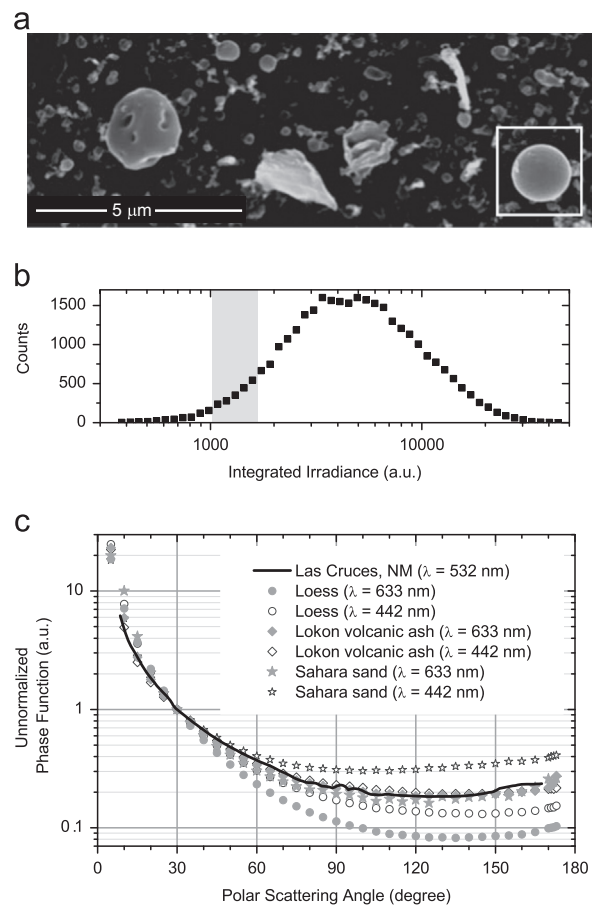
a

b

c

Fig. 3. (a) Scanning electron microscope images of collected atmospheric aerosol particles from experimental run displaying variations in particle shape. Inset: Highly spherical particle from another region (same scale). (b) Histogram of integrated scattering intensities of all atmospheric particles. The shaded region represents the range of scattering intensities (25th to 75th percentile) for 1 μm polystyrene spheres. (c) Ensemble average phase function for atmospheric particles obtained in this work (solid line) compared with the phase functions measured by Volten et al. [8].
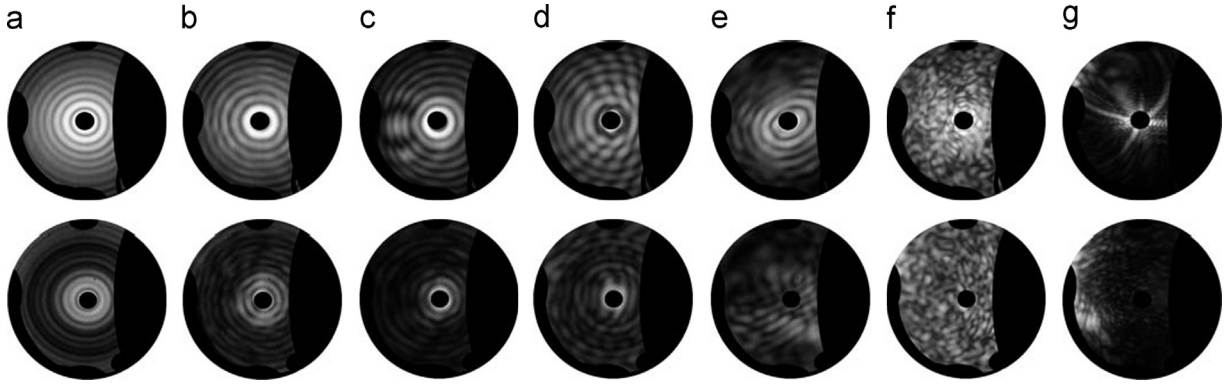
Fig. 4. Forward (top row) and backward (bottom row) scattering hemispheres from unknown atmospheric aerosol particles. To emphasize the features, a logarithmic scale is used and the backward scattering intensities are scaled by a factor of two as compared with the forward scattering intensities. Postulated particle shapes based on scattering patterns are (a) sphere, (b) inhomogeneous sphere or sphere with perturbed surface, (c) sphere with inclusion, (d) sphere with inclusion or merged spheres, (e) deformed sphere (i.e. spheroid) (f) complex aggregate, and (g) crystal.

hemisphere of Fig. 4(b) suggests a sphere-like particle but perhaps with inhomogeneous composition or a perturbed (rough) surface. Fig. 4(c) looks similar to scattering patterns of droplets with inclusions [29,30]. Fig. 4(d) might be a droplet with a large inclusion, but also looks similar to some recent simulation work exploring the scattering of merged spheroids [31]. The elliptical shaped near forward scattering of Fig. 4(e) suggests it is a spheroidal shaped particle [29,32]. The speckle pattern in Fig. 4(f) is known to represent morphological complexity [33] and might be an aggregate [34]. The scattering in the forward hemisphere of Fig. 4(g) suggests a crystalline particle shape [35]. This manual characterization approach would be too daunting for all 31 407 TAOS patterns. Thus automated image analysis techniques are utilized to classify and characterize the TAOS patterns, as is discussed in Section 5.

The integrated irradiance for a single TAOS pattern provides a crude estimate of particle size [36]. A histogram of these integrated irradiances for all detected TAOS patterns is shown in Fig. 3(b). The range of values for 1 μm PSL spheres are indicated by the grayed region. A majority of the integrated irradiances have higher values than the integrated irradiances of PSL spheres. This is to be expected since the concentrator disproportionally samples particle larger than 1 μm. In addition, there is a fairly large range of integrated irradiance values for virtually identical PSL spheres. As discussed in Section 2, this fluctuation corresponds to variations in the intensity of the incident beam illuminating the particles from shot-to-shot. Particle sizing is discussed in more detail in Section 5.

4. Scattering phase function

The aerosol scattering phase function represents the angular distribution of scattered light by an aerosol (i.e. an ensemble of aerosol particles) and is critical to remote sensing retrievals [37]. Following the notation and definitions in Bohren and Huffman [38], the scattering phase function, $p(\theta)$, is defined as

$$p(\theta) = \frac{1}{C_s} \frac{dC_s}{d\Omega},\qquad(1)$$

where C_s is the scattering cross section, Ω is solid angle, and $dC_s/d\Omega$ is the differential scattering cross section. These quantities are related by

$$C_s = \oint \frac{dC_s}{d\Omega} d\Omega.\qquad(2)$$

The differential scattering cross section, $dC_s/d\Omega$, can be determined from measurements of the irradiance:

$$\frac{dC_s}{d\Omega} = \frac{r^2}{I_i} I_s\qquad(3)$$

where I_s is the scattered intensity (i.e. detected irradiance), I_i is the incident intensity, and r is the distance to the detector.

For the TAOS apparatus, the detected irradiance is measured for individual particles rather than an ensemble of particles. However, in the single scattering regime, the irradiance of the ensemble is the sum of all the individual particle irradiances:

$$I_s(\theta) = \sum_{j=1}^{N} I_j(\theta)\qquad(4)$$

where $I_j(\theta)$ is the irradiance of particle j averaged over detected azimuthal angle ϕ and N is the total number of particles. Note that averaging over ϕ represents averaging over different scattering planes. This is in contrast to polar nephelometer measurements that detect irradiance in a single scattering plane from an ensemble of particles. We did not explicitly test whether our statistics are sufficient as is done when more of the elements of the scattering matrix are measured [39].

By combining Eqs. (1)–(4), the phase function of the ensemble is shown to be proportional to the summation of measured single particle irradiance:

$$p(\theta) = \frac{r^2}{C_s I_i} \sum_{j=1}^{N} I_j(\theta).\qquad(5)$$

We are unable to determine the absolute values of the scattering phase function since our experimental geometry does not measure the scattering light in the near forward ($\theta < 9°$) or near backward ($\theta > 167°$) directions. Hence, we cannot calculate the differential scattering cross

section $dC_s/d\Omega$ for all angles and thus the scattering cross section C_s is unknown. Instead, when making comparisons, we normalize our measured phase function to be 1 when θ is $30°$ following the work of others [8].

The aerosol phase function calculated from all 31 407 collected TAOS patterns is shown in Fig. 3(c). We compare our phase function with measurements made by Volten et al. [8] of mineral aerosol samples composed of super-micron particles since the distribution of integrated irra-diances in Fig. 3(b) indicates that the average diameter of our sampled particles is greater than 1 µm. The shape of our phase function is in good agreement with these measured phase functions as is evident in Fig. 3(c). This suggests that our sampled aerosol is composed of mainly non-spherical particles. We do not have a physical reason why our phase function appears most similar to Lokon volcanic ash as compared with the other samples mea-sured by Volten et al. [8]. Finally, it is important to stress that the TAOS apparatus' sampling rate is size dependent thus the collection of particles sampled is not representa-tive of the actual size distribution; the measured phase function is not representative of the actual aerosol phase function in Las Cruces, NM.

To decompose our phase function into contributions from subpopulations of particles, we note that the sum-mation in Eq. (5) over all N particles can be represented as a summation over subpopulations. For example, if the ensemble is divided into two subpopulations A and B with N_A and N_B particles respectively, then the phase function becomes

$$p(\theta) = \frac{r^2}{C_s I_i}\left(\sum_A I_j(\theta) + \sum_B I_j(\theta)\right) \tag{6}$$

where I_j is the irradiance of particle j averaged over azimuthal angle ϕ and $N_A + N_B = N$. To facilitate compar-isons between subpopulations, we normalize the summa-tion by the number of patterns summed and label this quantity $p_A^*(\theta)$:

$$p_A^*(\theta) = \frac{1}{N_A}\sum_A I_j(\theta). \tag{7}$$

The relationship between the actual scattering phase function of subpopulation A and this function is

$$p_A(\theta) = \frac{N_A r^2}{C_A I_i} p_A^*(\theta) \tag{8}$$

where C_A is the scattering cross section of subpopulation A. Thus $p_A^*(\theta)$ is proportional to the phase function $p_A(\theta)$. We therefore refer to it as the unnormalized phase function, although ensemble-averaged single-particle azimuthal-averaged scattered intensity might be a more accurate term.

5. Morphology characterization

5.1. Particle asphericity

Particle morphology can be discerned from the TAOS patterns as is evident from the analysis of TAOS images in Section 3. To automate the image analysis, variations of irradiance around the azimuthal angle ϕ can be used to

classify particle by shape [40,21,41,20]. In particular, Cotton et al. [20] were able to distinguish sea-salt particles (deliquesced salt solution droplets in a humid marine boundary layer) from mineral dust particles by measuring the asphericity factor A_f from light scattering of individual particles [20]. For this instrument, light was captured over forward-scattering angle of $9°$–$20°$ and recorded into 24 bins uniformly spaced around the azimuthal angle ϕ. The asphericity factor is then given by

$$A_f = \frac{k\sqrt{\sum_{i=1}^{n}(\overline{S}-S_i)^2}}{\overline{S}}, \tag{9}$$

where S_i is the detected irradiance of the ith bin, n is the total number of bins (i.e. 24), and k is a scale factor ($k = 100/\sqrt{n^2-n}$) so that $A_f < 100$. Spherical particles result in low A_f; non-spherical particles result in high A_f. Cotton et al. found an A_f of about 10 to be the threshold value between spherical sea-salt aerosol particles and non-spherical desert dust aerosol particles. Following this work, we calculate A_f for all TAOS patterns from forward scattered light ($15° < \theta < 25°$) using 24 bins spanning $360°$ in ϕ. A TAOS pattern with a low asphericity factor of 1 and a TAOS pattern with a high asphericity factor of 28 are shown as insets in Fig. 5. Matching expectations, the low A_f TAOS pattern appears to be from a spherical particle whereas the high A_f TAOS pattern appears to be from an elongated particle such as a fiber [42]. A histogram of A_f values for all TAOS patterns is also shown in Fig. 5. The A_f histogram has a peak value around an A_f of 10 and is somewhat normally distributed except for a side arm at low A_f.

Visual inspection confirms that TAOS patterns with low asphericity factors ($A_f < 3$) are spherical particles based on the presence of concentric rings in the forward and back-ward scattering hemispheres. Furthermore, visual inspec-tion confirms that TAOS patterns with high asphericity factors ($A_f > 11$) are non-spherical particles based on the lack of concentric rings in the TAOS pattern. However, there is a range of A_f values ($3 < A_f < 10$) where TAOS patterns represent a mix of spherical and non-spherical particles. Two factors contribute to this inability to dis-criminate between spherical and non-spherical particles. First, particle position misplacement (particle trajectory
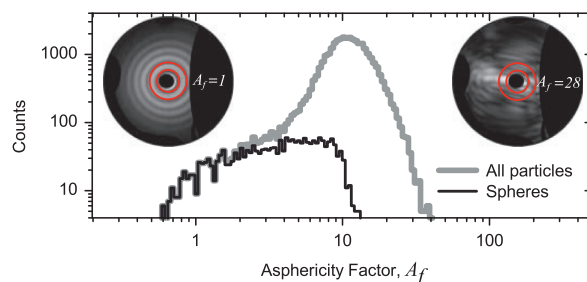
Fig. 5. Histogram of asphericity factor, A_f, for all TAOS patterns from over 30 000 atmospheric aerosol particles. Example patterns of low A_f (left) and high A_f (right) where red rings indicate minimum and maximum polar scattering angles used in calculating A_f. (For interpretation of the references to color in this figure caption, the reader is referred to the web version of this article.)

slightly displaced from the first focal point of the elliptical reflector) results in a higher A_f for spherical particles. In particular, if the mapping of θ and ϕ onto the ICCD pixels is slightly inaccurate, an artificial variation in irradiance can occur around the azimuthal angle ϕ. Second, TAOS patterns of non-spherical particle with dense uniform speckle display low A_f although they are not homogeneous spheres. For example, the TAOS pattern of a non-spherical particle shown in Fig. 4(f) has a relatively low A_f of 5. Thus TAOS patterns composed of dense speckle, like those captured from densely packed aggregates having an overall spherical shape [34,23], could have relatively low A_f since there is little variation in the average irradiance of each binned area. Thus for our apparatus, A_f cannot differentiate between homogeneous spherical particles and highly inhomogeneous particles that have an overall spherical shape.

5.2. Spherical classification

With the inability of A_f to differentiate between spherical and non-spherical particles, other image analysis routines were explored. Visual inspection of the TAOS patterns reveals that the backward scattering hemisphere is particularly sensitive to particle sphericity. For example, of the TAOS patterns displayed in Fig. 4, only Fig. 4(a) is thought to be a homogeneous sphere and is also the only pattern with concentric rings in the backscattering hemisphere. To quantify the presence or absence of these concentric rings, we use an autocorrelation analysis technique previously developed to distinguish between living cells using TAOS patterns [43].

Briefly, we plot the irradiance $(98° < \theta < 167°,\ 57° < \phi < 290°)$ in Cartesian coordinates as shown in left column of Fig. 6(a). The logarithm of the irradiance is calculated to reduce the dynamic range and minimize skewing our results towards the brightest rings. A top-hat filter is applied to remove the uneven background and emphasize the ring structure. Finally the two-dimensional autocorrelation function

$$Corr_j(\Delta\theta, \Delta\phi) = \frac{\langle I'_j(\theta,\phi)I'_j(\theta + \Delta\theta, \phi + \Delta\phi)\rangle}{\langle I'_j(\theta,\phi)\rangle^2} - 1 \qquad (10)$$

is calculated from these ring-enhanced TAOS patterns $I'_j(\theta,\phi)$. Example of autocorrelation functions are shown in right column of Fig. 6(a). As is evident, the shape of the central peak correlates well with the presence or absence of ring structure in the TAOS pattern. When rings are present, the central peak is much wider along $\Delta\phi = 0$ as compared with $\Delta\theta = 0$. We quantify this shape by calculating the ratio of the values of full-width at half maximum (FWHM) of the central peak at $\Delta\theta = 0$ and at $\Delta\phi = 0$.

Visual inspection confirms that the FWHM ratio is an excellent feature to classify spheres. For example, the three TAOS patterns shown in Fig. 6 represent the transition from a spherical homogeneous particle to a sphere-like particle to a highly non-spherical or highly inhomogeneous particle. All the patterns have relatively low asphericity factors in which the spherical particle has the lowest A_f value of 1 and the non-spherical particle and sphere-like
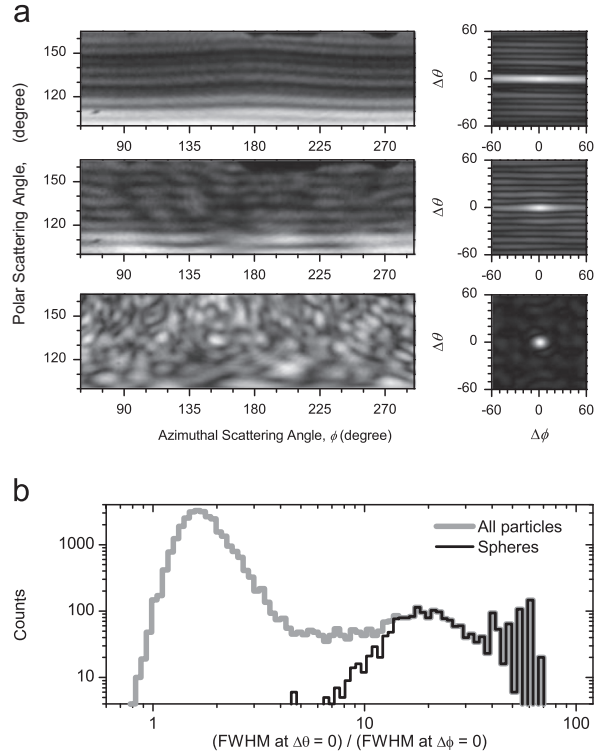

Fig. 6. (a) Left column: irradiance distributions mapped from Fig. 4(a), (b), and (f) (from top to bottom) onto Cartesian coordinates. These patterns all have low asphericity factors ($A_f = 2$, 7, and 5). Right column: corresponding two-dimensional autocorrelation functions of angular distributions after preprocessing (see Section 5.2). (b) Histogram of ratio values of full width at half maximum (FWHM) of autocorrelation function at $\Delta\theta = 0$ to FWHM of autocorrelation function at $\Delta\phi = 0$. FWHM ratios for TAOS patterns shown in (a) are 19, 7, and 1 from top to bottom.

particle have both relatively low A_f values of 7 and 5 respectively. The FWHM ratio clearly distinguishes this range of sphericity with values of 19 (sphere), 7 (sphere-like), and 1 (non-spherical or highly inhomogeneous particle). Furthermore, the autocorrelation analysis approach appears to be less sensitive to slight particle misplacement. A histogram of the values of FWHM ratio for all TAOS patterns is shown in Fig. 6. The high-frequency oscillations at large FWHM ratios are artifacts of the analysis due to sampling quantization effects.

We found that the FWHM ratio can distinguish between TAOS patterns of homogeneous spherical particles and TAOS patterns of non-spherical or highly inhomogeneous particles. However, we did not find a single threshold value that can clearly distinguish between TAOS patterns of spheres and sphere-like particles or between sphere-like particles and non-spherical/highly inhomogeneous particles. Therefore, we manually inspected and sorted all patterns with FWHM ratios greater than 3. Only patterns with concentric continuous rings in the forward and backward scattering hemispheres were labeled as spheres. The distribution of A_f values and FWHM ratios of TAOS patterns of spheres are shown in Figs. 5 and 6 respectively.

5.3. Particle sizing

It is known that the scattering cross section for large spheres scales with projected area [38], thus the integrated measured irradiance of our TAOS patterns might provide particle size information. However, in the size parameter range for our sampled size distribution (5–50 based on collection efficiencies of apparatus), the scattering cross section of spheres varies by as much as a factor of two from the predicted linear scaling behavior. Furthermore the majority of our particles is not spherical and this impacts the cross section as well [44]. Finally, fluctuations in the incident intensity from shot-to-shot (see Section 2) and non-complete coverage of detected scattering angles adds significant uncertainty in measuring the scattering cross section. However, even a crude estimate of particle size would greatly benefit our analysis. Our approach is to use the ring spacing (also known as the ripple structure [38]) in the TAOS patterns of spherical particles to estimate their diameter [45] and then to determine an empirical relationship for these spherical particles between integrated irradiance of the TAOS pattern and diameter determined from the ring spacing. This empirical formula converts the integrated irradiance of all TAOS patterns into an estimate of equivalent spherical particle diameter.

For a spherical particle with a large phase shift parameter $\rho = 2kR|m-1|$, where $k = 2\pi/\lambda$, R is the sphere radius, and m is the relative refractive index, the spacing of the rings is equal to π/kR [45]. Therefore, the diameter D of a spherical particle can be calculated from the average spacing between concentric rings $\delta\theta$:

$$D = \frac{2\pi}{k\delta\theta}. \tag{11}$$

Autocorrelation analysis discussed in Section 5.2 is used to estimate the spacing of concentric rings $\delta\theta$ in a TAOS pattern. In particular, an estimate of $\delta\theta$ is the location of the first peak away from the central maximum along $\Delta\theta$. To increase the range of $\delta\theta$ values measurable using the autocorrelation analysis, we analyzed an angular range ($18° < \theta < 167°$, $103° < \phi < 167°$) which has both large θ coverage and irradiance values at all angles.

The observed relationship between integrated irradiance and diameter determined from ring-spacing is shown in Fig. 7. Since the scattering cross section of large spheres scales as D^2, a power law fit is explored and the best fit is found to be $D^{1.4}$. The smaller exponent is expected since our apparatus does not measure the very near forward scattered light which constitutes a larger fraction of the total scattered light as size increases. This empirical formula,

$$D = (7.06 \times 10^{-3})I_{int}^{1/1.4}, \tag{12}$$

is then used to convert the integrated irradiance I_{int} of all TAOS patterns (spheres and non-spheres) into an equivalent spherical particle diameter D.

6. Results and discussions

Among all shapes, the scattering of light from homogeneous spherical particles is often the most anomalous [46].
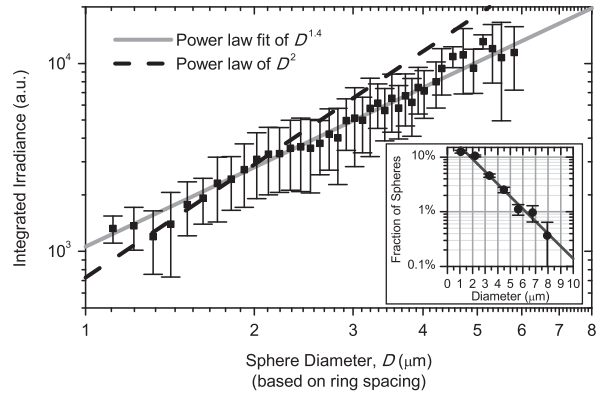

Fig. 7. Observed relationship between integrated irradiance and diameter of spherical particles, where the diameter is determined from ring spacing in scattering pattern. Empirical relationship is determined by fitting to power law. Inset: Fraction of spherical particles as a function of size. Line shows decaying exponential fit. Particle size was estimated from integrated irradiance.

Thus modeling the complex morphology of atmospheric aerosol particles using only homogeneous spheres greatly hinders the applicability of the model. If ignored, non-sphericity can significantly affect the results of remote sensing retrievals of refractive index, size, and aerosol optical thickness [47]. A critical development in the evolution of modeling scattered light from an aerosol layer is to represent an aerosol as a mix of non-spherical and spherical particles [11,13]. Thus we investigated the fraction of spherical particles in our sampled aerosol. Rather than calculating a single sphericity fraction for the entire size distribution as is often done in remote sensing applications, we determined how the fraction of spherical particles varies as a function of size. The results shown in the inset of Fig. 7 suggest that the fraction of spherical particles is not constant across our sampled size distribution, but falls off exponentially, $e^{D/\xi}$, with increasing diameter D and decay constant ξ. The best exponential fit for our sampled aerosol occurs when ξ is 1.9 μm. A similar trend of decreasing spherical fraction was evident in other studies as well such as sampled aerosol from the Baltimore–Washington metroplex [15] and aerosol particles sampled in the Southeastern Aerosol and Visibility Study (SEAVS) [21]. This suggests that adding an additional free parameter, sphericity decay constant, could improve the accuracy of remote sensing retrievals, although more in situ experiments are needed to verify this behavior across a spatially and temporally diverse range of aerosols.

Fig. 8 shows the main result from experimental data analysis, the dependence of scattering phase functions on the particle morphology of atmospheric aerosol particles. The dataset is subdivided by particle size into 6 size ranges so that each range had close to or more than 3000 TAOS patterns (see Table 1). The unnormalized phase function (see Section 4 for definition) of each size range is displayed in Fig. 8(a). The disappearance of the enhanced backward scattering (i.e. glory) with increasing particle size correlates well with our finding that the fraction of spherical particles diminishes with increasing particle size. In order to see how the phase function varies with particle
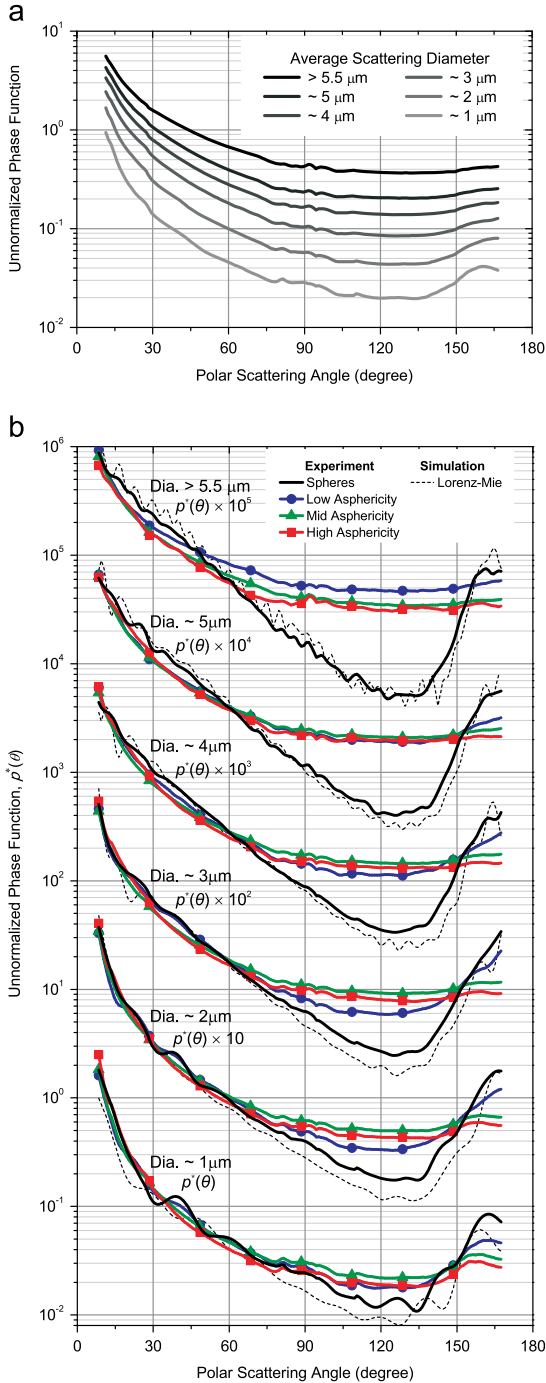
Fig. 8. (a) Average phase functions for different size ranges. Range for each size is $\pm 0.5\ \mu m$ except for the largest size where the range is 5.5–14 μm with a mean of 7 μm. (b) Average phase functions for various asphericity bins in different size ranges. Dashed lines represent the phase functions of spherical particle simulated with Lorenz–Mie theory.

particles and non-spherical particles within each size range are plotted in Fig. 8(b). As a check of our experimental approach, the phase function of spherical particles obtained from experimental measurement is compared with simulation based on Lorenz–Mie theory (dashed lines). For the simulation, the distribution of particle diameters is determined from the integrated irradiance of the TAOS patterns, the refractive index of each sphere is set to 1.5 based on previous work [15], and the absorption was set to zero. The only free parameter adjusted to match the experimental results is an overall scale factor, where the same scale factor is utilized for all size distributions. The Lorenz–Mie simulation matched well with our experimentally measured phase functions of spherical particles over all size ranges, giving us confidence in our approach.

The TAOS patterns of non-spherical/inhomogeneous particles are further subdivided into 5 bins based on the asphericity factor A_f. The range of values of each A_f bin as well as the fraction of patterns in each bin is displayed in Table 1. The first A_f bin ($A_f < 6$) contains TAOS patterns of non-spherical/inhomogeneous particles with A_f values equivalent to spheres (see Fig. 5). In contrast, the last A_f bin ($A_f > 17$) contains TAOS patterns of non-spherical/inhomogeneous particles with A_f values that are significantly different from spheres. The unnormalized scattering phase function for these bins are calculated and displayed in Fig. 8(b). For clarity, we only graphed the unnormalized phase function of the first, middle, and last A_f bins. Two trends are readily apparent. First, as size increases, the scattering phase function of homogeneous spherical particles becomes quite distinct from all other phase functions. This provides further support for the commonly held belief that spherical particles exhibit scattering behavior unique among particle shape spectrum [46]. Second, the phase functions of non-spherical/inhomogeneous particles for different A_f bins do not vary considerably within each size range. These two results support the current practice in remote sensing retrievals to differentiate between spherical and non-spherical particles while not further characterizing the morphology of the non-spherical particles. For example, in AERONET inversions of spectral and angular photopolarimetric retrievals, the fraction of spherical particles is a free parameter while the shape distribution of spheroids is fixed. Our results suggest that the optical properties (i.e. the scattering phase function) of non-spherical particles vary little with particle shape (i.e. asphericity factor A_f). This is in contrast to recent simulations work suggesting that shape distributions of spheroids are important in modeling the measured optical properties of mineral dust [16]. However, their conclusion was based on fitting the full scattering matrix rather than just a single matrix element. Indeed, when Merikallio et al. [16] did just fit the scattering phase function, they found all the mineral samples were best modeled with an equiprobable distribution of spheroid shapes.

Other trends are apparent from the unnormalized scattering phase function. For example, for all size ranges except for the $D > 5.5\ \mu m$, glory is evident in the backscattering at low A_f suggesting that a fraction of these particles are sphere-like in shape perhaps with inclusions or rough surfaces. For the particles in the largest size range

asphericity at different size ranges, TAOS patterns in each size bin are subdivided into two groups (1) homogeneous spherical particles and (2) non-spherical and/or inhomogeneous particles. The corresponding unnormalized scattering phase functions of the homogeneous spherical

Table 1
Frequency of occurrence for different scattering patterns.

Particle diameter (μm)	Size parameter	Patterns	Spheres (%)	Non-spherical particles (%)				
				$(A_f < 6)$	$(6 < A_f < 9)$	$(9 < A_f < 12)$	$(12 < A_f < 17)$	$(A_f > 17)$
1 ± 0.5	~7	3255	11	5	17	26	27	13
2 ± 0.5	~12	9452	11	5	17	30	26	11
3 ± 0.5	~18	7785	5	4	20	34	27	10
4 ± 0.5	~23	4901	3	3	26	37	25	7
5 ± 0.5	~29	2754	2	4	30	38	22	5
$5.5–14$	~41	3269	< 1	7	43	34	14	2

$(D > 5.5\ \mu m)$ not only is the glory absent, but also is the phase function considerably flat even for low A_f non-spherical particles. A possible explanation is that particles in this bin (i.e. large, non-spherical, low A_f) have overall spherical shape with highly inhomogeneous composition such as a tightly packed aggregate. As discussed in Section 6, such particles have fairly uniform azimuthal scattering and thus low A_f values while being morphologically as well as optically different from homogeneous spheres.

7. Summary

In this work, we devised a powerful experimental technique that simultaneously measures both optical properties (i.e. the scattering phase function) and morphological features (i.e. asphericity and size) of individual atmospheric particles. Central to our approach was the measurement of two-dimensional angular optical scattering (TAOS) patterns that have both high angular resolution and large angular coverage of the forward and backward scattering hemispheres. As a proof-of-concept, our apparatus measured TAOS patterns of over 3000 atmospheric aerosol particles during an 18-h period in January 2007 in the Las Cruces, NM. To characterize the shape of the sampled aerosol particles, the asphericity factor A_f was calculated for each TAOS pattern. Patterns representative of scattering from homogeneous spherical particles had the lowest A_f values, but patterns composed of fairly uniform dense speckle, which do not represent scattering from homogeneous spheres, also had relatively low values of the asphericity factor A_f. Autocorrelation analysis of TAOS patterns was used to further differentiate between TAOS patterns of homogeneous spherical particles and sphere-like particles that are either slightly non-spherical in shape or inhomogeneous in composition. However, there was no single threshold value for all particle size to distinguish between TAOS patterns of homogeneous spheres and those of sphere-like particles, thus we resorted to manually sorting these two classes of TAOS patterns. The particle size was estimated from the integrated irradiance of the TAOS patterns. We found that the fraction of spherical particles decreased exponentially from ~10% for particles around 1 μm in diameter to < 1% for particles greater than 5 μm in diameter.

The unnormalized phase function, which is proportional to the scattering phase function, is determined by averaging TAOS patterns. The phase function of spherical atmospheric particles is shown to become more distinct from the phase function of non-spherical atmospheric particles as particle size increases, while the phase function of non-spherical particles averaged over different ranges of A_f did not vary considerably. These results support the commonly held belief that spherical particles exhibit scattering behavior unique among particle shape spectrum [46]. Furthermore, it validates the current practice in remote sensing retrievals to differentiate between spherical and non-spherical particles while not further characterizing the morphology of the non-spherical particles [13]. It is important to note that our work focuses on the single element of the scattering matrix most important to climate research, but it is likely that other unmeasured elements of the scattering matrix will show a stronger dependence upon specific characterization of non-sphericity [16]. The collected TAOS patterns and calculated phase functions are available from the lead author upon request.

References

[1] Charlson RJ, Schwartz SE, Hales JM, Cess RD, Coakley JA, Hansen JE, et al. Climate forcing by anthropogenic aerosols. Science 1992;255: 423–30.

[2] Forster P, Ramaswamy V, Artaxo P, Berntsen T, Betts R, Fahey DW, et al. Changes in atmospheric constituents and in radiative forcing. In: Solomon S, Qin D, Manning M, Chen Z, Marquis M, Averyt KB, et al., editors. Climate change 2007: the physical science basis. contribution of working group I to the fourth assessment report of the intergovernmental panel on climate change. Cambridge, UK and New York, NY, USA: Cambridge University Press; 2007. p. 129–234.

[3] Mian C, Kahn RA, Schwartz SE, editors. CCSP2009: atmospheric aerosol properties and climate impacts, A report by the U.S. Climate Change Science Program and the Subcommittee on Global Change Research. Washington, DC, USA: National Aeronautics and Space Administration; 2009.

[4] Nousiainen T. Optical modeling of mineral dust particles: a review. J Quant Spectrosc Radiat Transf 2009;110:1261–79.

[5] King MD, Byrne DM, Herman BM, Reagan JA. Aerosol size distributions obtained by inversion of spectral optical depth measurements. J Atmos Sci 1978;35:2153–67.

[6] Nakajima T, Tonna G, Rao RZ, Boi P, Kaufman Y, Holben B. Use of sky brightness measurements from ground for remote sensing of particulate polydispersions. Appl Opt 1996;35:2672–86.

[7] West RA, Doose LR, Eibl AM, Tomasko MG, Mishchenko MI. Laboratory measurements of mineral dust scattering phase function and linear polarization. J Geophys Res 1997;102:16871–81.

[8] Volten H, Munoz O, Rol E, de Haan JF, Vassen W, Hovenier JW, et al. Scattering matrices of mineral aerosol particles at 441.6 nm and 632.8 nm. J Geophys Res 2001;106:17375–401.

[9] Liu YG, Arnott WP, Hallett J. Particle size distribution retrieval from multispectral optical depth: influences of particle nonsphericity and refractive index. J Geophys Res 1999;104:31753–62.

[10] Dubovik O, Holben B, Eck TF, Smirnov A, Kaufman YJ, King MD, et al. Variability of absorption and optical properties of key aerosol types observed in worldwide locations. J Atmos Sci 2002;59:590–608.

[11] Herman M, Deuze JL, Marchand A, Roger B, Lallart P. Aerosol remote sensing from POLDER/ADEOS over the ocean: improved retrieval using a nonspherical particle model. J Geophys Res 2005;110: D10S02.

[12] Kalashnikova OV, Kahn R, Sokolik IN, Li WH. Ability of multiangle remote sensing observations to identify and distinguish mineral dust types: optical models and retrievals of optically thick plumes. J Geophys Res 2005;110:D18S14.

[13] Dubovik O, Sinyuk A, Lapyonok T, Holben BN, Mishchenko M, Yang P, et al. Application of spheroid models to account for aerosol particle nonsphericity in remote sensing of desert dust. J Geophys Res 2006;111:D11208.

[14] Nousiainen T, Kahnert M, Veihelmann B. Light scattering modeling of small feldspar aerosol particles using polyhedral prisms and spheroids. J Quant Spectrosc Radiat Transf 2006;101:471–87.

[15] Aptowicz KB, Pinnick RG, Hill SC, Pan YL, Chang RK. Optical scattering patterns from single urban aerosol particles at Adelphi, Maryland, USA: a classification relating to particle morphologies. J Geophys Res 2006;111:D12212.

[16] Merikallio S, Lindqvist H, Nousiainen T, Kahnert M. Modelling light scattering by mineral dust using spheroids: assessment of applicability. Atmos Chem Phys 2011;11:5347–63.

[17] Meland B, Alexander JM, Wong CS, Grassian VH, Young MA, Kleiber PD. Evidence for particle size-shape correlations in the optical properties of silicate clay aerosol. J Quant Spectrosc Radiat Transf 2012;113:549–58.

[18] Munoz O, Hovenier JW. Laboratory measurements of single light scattering by ensembles of randomly oriented small irregular particles in air: a review. J Quant Spectrosc Radiat Transf 2011;112: 1646–57.

[19] Johnson B, Turnbull K, Brown P, Burgess R, Dorsey J, Baran AJ, et al. In situ observations of volcanic ash clouds from the FAAM aircraft during the eruption of Eyjafjallajokull in 2010. J Geophys Res 2012;117:D00U24. http://dx.doi.org/10.1029/2011JD016760.

[20] Cotton R, Osborne S, Ulanowski Z, Hirst E, Kaye PH, Greenaway RS. The ability of the Small Ice Detector (SID-2) to characterize cloud particle and aerosol morphologies obtained during flights of the FAAM BAe-146 research aircraft. J Atmos Oceanic Technol 2010;27: 290–303.

[21] Dick WD, Ziemann PJ, Huang PF, McMurry PH. Optical shape fraction measurements of submicrometre laboratory and atmospheric aerosols. Meas Sci Technol 1998;9:183–96.

[22] Holler S, Pan YL, Chang RK, Bottiger JR, Hill SC, Hillis DB. Two-dimensional angular optical scattering for the characterization of airborne microparticles. Opt Lett 1998;23:1489–91.

[23] Pan YL, Aptowicz KB, Chang RK, Hart M, Eversole JD. Characterizing and monitoring respiratory aerosols by light scattering. Opt Lett 2003;28:589–91.

[24] Fernandes GE, Pan YL, Chang RK, Aptowicz K, Pinnick RG. Simultaneous forward- and backward-hemisphere elastic-light-scattering patterns of respirable-size aerosols. Opt Lett 2006;31:3034–6.

[25] Pan YL, Pinnick RG, Hill SC, Rosen JM, Chang RK. Single-particle laser-induced-fluorescence spectra of biological and other organic-carbon aerosols in the atmosphere: measurements at New Haven, Connecticut, and Las Cruces, New Mexico. J Geophys Res 2007;112: D24S19.

[26] Pinnick RG, Hill SC, Pan YL, Chang RK. Fluorescence spectra of atmospheric aerosol at Adelphi, Maryland, USA: measurement and classification of single particles containing organic carbon. Atmos Environ 2004;38:1657–72.

[27] Pan YL, Holler S, Chang RK, Hill SC, Pinnick RG, Niles S, et al. Single-shot fluorescence spectra of individual micrometer-sized bioaerosols illuminated by a 351- or a 266-nm ultraviolet laser. Opt Lett 1999;24:116–8.

[28] Junker C, Sheahan JN, Jennings SG, O'Brien P, Hinds BD, Martinez-Twary E, et al. Measurement and analysis of aerosol and black carbon in the southwestern United States and Panama and their dependence on air mass origin. J Geophys Res 2004;109:D13201.

[29] Secker DR, Kaye PH, Greenaway RS, Hirst E, Bartley DL, Videen G. Light scattering from deformed droplets and droplets with inclusions. I. Experimental results. Appl Opt 2000;39:5023–30.

[30] Videen G, Sun WB, Fu Q, Secker DR, Greenaway RS, Kaye PH, et al. Light scattering from deformed droplets and droplets with inclusions. II. Theoretical treatment. Appl Opt 2000;39:5031–9.

[31] Petrov D, Shkuratov Y, Videen G. The Sh-matrix method applied to light scattering by two merging spheroids. J Quant Spectrosc Radiat Transf 2010;111:1990–9.

[32] Petrov D, Shkuratov Y, Videen G. Application of the Sh-matrices method to light scattering by spheroids. J Opt 2010;12:095701.

[33] Mishchenko MI, Tishkovets VP, Travis LD, Cairns B, Dlugach JM, Liu L, et al. Electromagnetic scattering by a morphologically complex object: Fundamental concepts and common misconceptions. J Quant Spectrosc Radiat Transf 2011;112:671–92.

[34] Holler S, Auger JC, Stout B, Pan Y, Bottiger JR, Chang RK, et al. Observations and calculations of light scattering from clusters of spheres. Appl Opt 2000;39:6873–87.

[35] Hirst E, Kaye PH. Experimental and theoretical light scattering profiles from spherical and nonspherical particles. J Geophys Res 1996;101:19231–5.

[36] Black DL, McQuay MQ, Bonin MP. Laser-based techniques for particle-size measurement: a review of sizing methods and their industrial applications. Prog Energ Combust 1996;22:267–306.

[37] Mishchenko MI, Travis LD, Kahn RA, West RA. Modeling phase functions for dustlike tropospheric aerosols using a shape mixture of randomly oriented polydisperse spheroids. J Geophys Res 1997;102:16831–47.

[38] Bohren CF, Huffman DR. Absorption and scattering of light by small particles. New York: Wiley; 1983.

[39] Hovenier J, van der Mee CVM. Testing scattering matrices: a compendium of recipes. J Quant Spectrosc Radiat Transf 1996;55: 649–61.

[40] Kaye PH, Alexander-Buckley K, Hirst E, Saunders S, Clark JM. A real-time monitoring system for airborne particle shape and size analysis. J Geophys Res 1996;101:19215–21.

[41] Hirst E, Kaye PH, Greenaway RS, Field P, Johnson DW. Discrimination of micrometre-sized ice and super-cooled droplets in mixed-phase cloud. Atmos Environ 2001;35:33–47.

[42] Kaye P. Spatial light-scattering analysis as a means of characterizing and classifying non-spherical particles. Meas Sci Technol 1998;9(2): 141–9. http://dx.doi.org/10.1088/0957-0233/9/2/002.

[43] Pan YL, Berg MJ, Zhang SSM, Noh H, Cao H, Chang RK, et al. Measurement and autocorrelation analysis of two-dimensional light-scattering patterns from living cells for label-free classification. Cytometry A 2011;79A:284–92.

[44] Redmond HE, Dial KD, Thompson JE. Light scattering and absorption by wind blown dust: theory, measurement, and recent data. Aeolian Res 2010;2:5–26.

[45] Sorensen CM, Shi D. Patterns in the ripple structure of Mie scattering. J Opt Soc Am A 2002;19:122–5.

[46] Mugnai A, Wiscombe WJ. Scattering from nonspherical Chebyshev particles. 3: Variability in angular scattering patterns. Appl Opt 1989;28:3061–73.

[47] Mishchenko MI, Cairns B, Kopp G, Schueler CF, Fafaul BA, Hansen JE, et al. Accurate monitoring of terrestrial aerosols and total solar irradiance: introducing the glory mission. Bull Am Meteorol Soc 2007;88:677–91.